# One-point statistics for turbulent wall-bounded flows at Reynolds numbers up to δ+ ≈ 2000

Juan A. Sillero, Javier Jiménez, and Robert D. Moser

## Additional information on Phys. Fluids

# One-point statistics for turbulent wall-bounded flows at Reynolds numbers up to $\delta^+ \approx 2000$

Juan A. Sillero,[1,a)] Javier Jiménez,[1] and Robert D. Moser[2]

[1]*School of Aeronautics, U. Politécnica de Madrid, 28040 Madrid, Spain*
[2]*Department of Mechanical Engineering and Institute for Computational Engineering and Sciences, University of Texas, Austin, Texas 78735, USA*

One-point statistics are presented for new direct simulations of the zero-pressure-gradient turbulent boundary layer in the range $Re_\theta = 2780$–$6680$, matching channels and pipes at $\delta^+ \approx 1000$–$2000$. For tripped boundary layers, it is found that the eddy-turnover length is a better criterion than the Reynolds number for the recovery of the largest flow scales after an artificial inflow. Beyond that limit, the integral parameters, mean velocities, Reynolds stresses, and pressure fluctuations of the new simulations agree very well with the available numerical and experimental data, but show clear differences with internal flows when expressed in wall units at the same wall distance and Reynolds number. Those differences are largest in the outer layer, independent of the Reynolds number, and apply to the three velocity components. The logarithmic increase with the Reynolds number of the maximum of the streamwise velocity and pressure fluctuations is confirmed to apply to experimental and numerical internal and external flows. The new simulations also extend to a wider range of Reynolds numbers, and to more than a decade in wall distance, the evidence for logarithmic intensity profiles of the spanwise velocity and of the pressure intensities. Streamwise velocity fluctuations appear to require higher Reynolds numbers to develop a clear logarithmic profile, but it is argued that the comparison of the available near-wall data with fluctuation profiles experimentally obtained by other groups at higher Reynolds numbers can only be explained by assuming the existence of a mesolayer for the fluctuations. The statistics of the new simulation are available in our website. © 2013 AIP Publishing LLC. [http://dx.doi.org/10.1063/1.4823831]

## I. INTRODUCTION

Internal and external wall-bounded turbulent flows have been subjects of intensive research because of their technological importance and fundamental physical interest, and, since the pioneering work of Kim, Moin, and Moser,[1] direct numerical simulations (DNS) have played a fundamental role in our understanding of their properties. With the increase of computer power, the Reynolds number of simulations has increased steadily, although initially mainly for channels. The Reynolds number of numerical boundary layers has increased more slowly because of the difficulties posed by their streamwise inhomogeneity and the need for high-quality inflow conditions. The same is true for pipes because of the challenge of finding a suitable representation for the flow near the pipe axis. Nevertheless, it is becoming possible to compare results for different flows at relatively high Reynolds numbers. In this paper we present a new simulation of the zero-pressure-gradient turbulent boundary layer at a Reynolds number, $Re_\theta \approx 6600$ ($\delta^+ \approx 2000$), comparable to those of the largest available channels,[2] and compare the results with the available experiments and simulations of internal and external flows.

a)sillero@torroja.dmt.upm.es

To correlate different flows we use the Kármán number, $\delta^+ = u_\tau \delta / \nu$, based on the kinematic viscosity $\nu$, on the streamwise-dependent friction velocity $u_\tau$, and on the flow thickness $\delta$, which is taken to be the half-width in channels, the 99% thickness in boundary layers,[3] and the radius in pipes.[4] The "+" superscript denotes normalization with $u_\tau$ and $\nu$. The Reynolds number $Re_\theta = U_\infty \theta / \nu$ is defined for boundary layers in terms of the momentum thickness $\theta$ and of the free-stream velocity $U_\infty$.

Our first goal is to characterize the initial development of the velocity statistics in experimentally or numerically tripped boundary layers. In the careful study by Erm and Joubert[5] of the effect of different experimental tripping devices, the authors conclude that the differences observed in the mean velocity profile disappear beyond $Re_\theta \approx 3000$. Likewise, Schlatter and Örlü[6] analyze the effect of different low-Reynolds-number trips on their DNS statistics, and show that a well-established boundary layer is attained at $Re_\theta \approx 2000$. On the other hand, Simens et al.[7] proposed that the turnover length, defined as the distance $L_{to} = U_\infty \delta / u_\tau$ by which eddies are advected during a turnover time $\delta / u_\tau$, provides a better description than the Reynolds number of how fast boundary layer simulations recover from synthetic inflow conditions. They found that at least one eddy-turnover is required for most flow scales to decorrelate from the inlet. Using the new data, we will compare the relative merits of the Reynolds number and of the turnover length as indicators of recovery, and we will show that the recovery length of the largest scales is considerable longer than the decorrelation length mentioned above.

Our second goal is to examine the universality of the mean and fluctuating velocity profiles in the near-wall and logarithmic regions, and to inquire on the similarities and differences between internal (channels and pipes) and external (boundary layers) flows. The universality of the velocity fluctuations in the inner layers has been analyzed before. The early expectations that the fluctuation intensities scale strictly in wall units[8] were eventually found to be incorrect,[2,9,10] and had, in any case, been shown to be unfounded by Townsend,[11] who noted that the wall-parallel velocities should include a Reynolds-number-dependent "inactive" contribution, associated with outer structures extending down to the viscous sublayer. The question has been extensively discussed over the last decade, both numerically and experimentally, but it is still not fully resolved. While most researchers find an increase of the near-wall intensities with the Reynolds number,[3,4,12–16] in agreement with Townsend[11] argument, one particular group does not, even at the highest Reynolds numbers experimentally available.[17,18] The steady increase of the Reynolds numbers of the simulations, which generally have fewer statistical and resolution uncertainties than experiments, will allow us to update the data on that point and, in the process, to examine the evidence for the logarithmic profiles of the intensities of the fluctuating velocities and of the pressure,[3,18] which were also predicted by Townsend.[11]

Because these near-wall effects are connected with outer structures,[11] they have to be examined together with the question of the differences between internal and external flows, which are predominantly outer effects. Jiménez and Hoyas,[3] after examining a wide range of experiments and numerical simulations, identified differences in the fluctuations of the transverse velocities (spanwise and wall-normal velocity components) and of the pressure. Those differences were confirmed by Buschmann and Gad-el-Hak[14] using additional data, and Jiménez et al.[15] later used DNSs of boundary layers and channels at $\delta^+ \approx 400$–700 to show that they could be explained by the effect of the large-scale intermittency in external flows. They found that the largest differences between the two kinds of flows are located just above the logarithmic layer ($y/\delta \approx 0.3$–0.5), where $y$ is the distance to the wall, but their limited Reynolds numbers prevented them from establishing the scaling of that distance. Similar results have been obtained more recently by Lee and Sung,[19] who compared DNSs of boundary layers and pipes at $\delta^+ \approx 930$. We will extend them to the higher Reynolds numbers of the present simulations, and clarify the behavior of the streamwise velocity fluctuations, which was unclear in previous studies.

The article is organized as follows. Section II describes the new boundary layer simulations. Section III examines the streamwise development length required for the initial recovery of boundary layers, while Sec. IV discusses one-point statistics, and compares them to existing numerical and experimental boundary layers, channels, and pipes. Conclusions are offered in Sec. V.

## II. NUMERICAL EXPERIMENTS

The boundary layer is simulated in a parallelepiped over a flat plate with periodic spanwise boundary conditions and non-periodic streamwise and wall-normal directions. The velocity components in the streamwise ($x$), wall-normal ($y$), and spanwise ($z$) directions are $u$, $v$, and $w$, respectively. The numerical code solves the primitive-variable formulation of the incompressible Navier-Stokes equations, using a fractional step method[20] to ensure mass conservation. Staggered three-points compact finite differences[21] are used for the spatial discretization of the derivatives in the $x$ and $y$ directions, except for the Poisson equation for the pressure, in which second-order finite differences are used. The representation in the spanwise direction is Fourier spectral, dealiased using the 2/3 rule, and time marching is a semi-implicit three-step Runge Kutta.[22] A detailed description of the problem formulation, the numerical scheme, and its validation can be found in Ref. 7.

Table I summarizes the simulation parameters for the different boundary layers used below. The simulation $BL_{2100}$ was discussed in Ref. 15, and is included here to allow comparison with experiments at lower Reynolds numbers. The simulation $BL_0$ was a first unsuccessful attempt to increase the Reynolds number up to $\delta^+ \approx 2000$. Its set-up is sketched in Figure 1(a). It is analogous to the older simulation $BL_{2100}$, but uses about fourteen times more grid points, over a higher Reynolds number range. The inflow boundary condition is generated using a version of the rescaling method in Ref. 23, in which the fluctuating velocities from a reference downstream plane $X_{rec}$ are used to create the incoming turbulence. The only minor deviation from the method in Ref. 23 is to use a $y$-dependent mapping to rescale the velocities from the reference plane to the inflow, instead of merging two individually scaled flow fields. The original rescaling method was found to generate unnatural bimodal fluctuation profiles that delayed the initial flow recovery. The recycling plane is

TABLE I. Parameters of the turbulent boundary layers discussed in the text. $L_x$, $L_y$, and $L_z$ are the box dimensions along the three axes. $N_x$, $N_y$, and $N_z$ are the collocation grid sizes. The momentum thickness $\theta$, the edge of the boundary layer $\delta$, and the friction velocity $u_\tau$ are taken at the middle of the box. $\widetilde{L}_x = \int_0^{L_x} [\, dx/(\delta U_\infty^+)]$ is the dimensionless length measured in eddy turn-overs. T is the total time over which statistics are compiled.

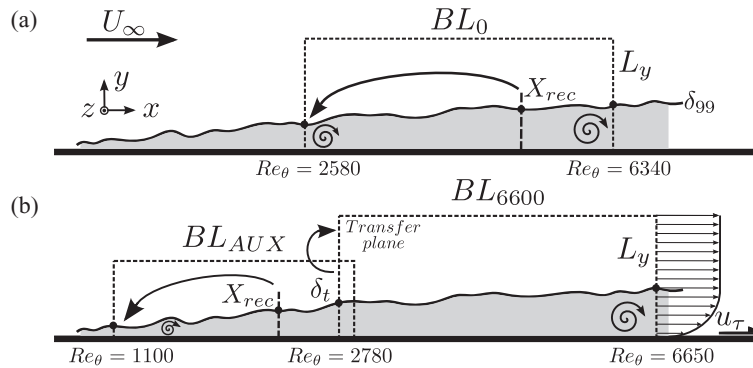| Case | $Re_\theta$ | $(L_x, L_y, L_z)/\theta$ | $\widetilde{L}_x$ | $\Delta x^+, \Delta y^+, \Delta z^+$ | $N_x, N_y, N_z$ | $Tu_\tau/\delta$ |
|---|---|---|---|---|---|---|
| $BL_{2100}$ | 617–2140 | $535 \times 29 \times 88$ | 3.25 | $6.10 \times 0.30 \times 4.1$ | $6145 \times 360 \times 1536$ | 21 |
| $BL_0$ | 2580–6340 | $534 \times 30 \times 67$ | 2.57 | $6.10 \times 0.30 \times 4.15$ | $16385 \times 711 \times 4096$ | 6.9 |
| $BL_{AUX}$ | 1100–2970 | $481 \times 47 \times 191$ | 2.61 | $13.00 \times 0.32 \times 7.28$ | $3585 \times 315 \times 2560$ | 27.6 |
| $BL_{6600}$ | 2780–6650 | $547 \times 29 \times 84$ | 2.68 | $7.00 \times 0.32 \times 4.07$ | $15361 \times 535 \times 4096$ | 11.5 |



FIG. 1. Sketches of the numerical simulation set-ups, including the Reynolds numbers achieved, and the nomenclature. Inflow conditions are generated using a recycled downstream velocity plane $\{u, v, w\}$ at $X_{rec}$, on which a rescaling technique is employed. (a) Single-domain computational box, used for $BL_{2100}$ and $BL_0$. (b) Double-domain computational box. The auxiliary low-resolution simulation $BL_{AUX}$ feeds the main simulation $BL_{6600}$. A plane located near the end of the first domain is transferred into the main high-resolution simulation.

located at $X_{rec} \approx 50\delta_{inlet}$, far enough downstream to avoid spurious periodicities due to the rescaling feedback.[7]

As will be seen below, $BL_0$ was found to be too short to develop completely within the box, especially for the larger flow scales. The problem was solved using the new computational set-up sketched in Figure 1(b), consisting of two simulation boxes running concurrently. The first box, $BL_{AUX}$, is intended to provide a realistic turbulent inflow for the larger scales of the main simulation $BL_{6600}$, and creates its own inflow using the same rescaling technique as $BL_0$. A velocity cross-plane located near the end of this first box is then transferred at each time step to the inlet of the second one.

The cost of $BL_{AUX}$ is marginal, because its purpose is to allow the development of the larger scales, and it does not need to be fully resolved. Even a linear factor of 2 in the two wall-parallel directions, which has very little influence except in the details of the vorticity dynamics, reduces the computational cost by a factor of 4, and a further reduction is possible because the boundary layer is thinner in the upstream part of the simulation, and the top of the domain can be made 25% lower than in the main box. Even after that reduction, the height ratio at the end of $BL_{AUX}$ is $L_y/\delta \approx 3.9$, compared to $L_y/\delta \approx 2.5$ for $BL_{6600}$. Both are larger than the ratio, $L_y/\delta > 2.4$, required to ensure that the free-stream velocity fluctuations are not constrained by the geometry of the computational box.[7] The resulting cost of the auxiliary simulation is about 8% of the main one.

The mean pressure gradient is controlled by imposing an $x$-dependent wall-normal velocity at the top of the computational box, estimated from the continuity equation as $V_\infty = U_\infty d\delta^*/dx$, where the displacement thickness $\delta^*$ is obtained from the empirical correlation in Ref. 24. The resulting pressure gradient is small, $\delta^* U_\infty^+ \partial_x U_\infty^+ \approx 10^{-3}$. Convective boundary conditions are applied at the exits of each of the two computational boxes, with minor adjustments to the outflow streamwise velocities to compensate any mass-flux variations resulting from the time-dependent inflows.[7] In incompressible flows, those adjustments can only occur through pressure pulses that can be shown to be confined to the largest flow scales. They have wavelengths of the order of the computational box, and amplitudes $\Delta p = -\dot{m}_i(L_x/L_y)$, where $\dot{m}_i$ is the temporal rate of change of the mass flow at the inlet. Because the box elongation $L_x/L_y$ is typically large, those pulses can severely contaminate the pressure statistics, even if their influence on the rest of the flow quantities is usually negligible because the pressure gradients involved are very weak. To minimize the fluctuations, the mass flux in $BL_{AUX}$ is kept constant by fixing the mean velocity profile at the inflow to a prescribed empirical one derived by matching inner and outer approximations across an overlap layer, as in Ref. 25. This ensures that the mass flux at the transfer plane of $BL_{AUX}$ remains constant, but unfortunately the same is not true at the inflow of $BL_{6600}$. That plane is generated by first interpolating the velocities of the transfer plane to the finer wall-normal grid of the main simulation, and then extrapolating the free stream to match the height of the new computational box. The first step conserves mass quite accurately, but the second one introduces small temporal variations because the velocity of the free stream, even if essentially uniform, varies slightly with time. In our case the flux variations were less than 1%, but they increased the root-mean-squared pressure fluctuations by more than 20%. This was avoided by rescaling the inflow profile of $BL_{6600}$ very slightly at each time step to keep its mass flux strictly constant.

The final simulation ran for a total of 45 million core hours in 32768 cores of a Blue Gene/P supercomputer with excellent scalability, using 8192 MPI nodes and four OpenMP threads per node. A complete description of the implementation and parallelization aspects can be found in Ref. 26.

## III. THE INITIAL DEVELOPMENT OF THE MEAN VELOCITY PROFILE

Experimental and numerical turbulent boundary layers are often tripped to avoid the slow natural transition from laminar flow, and measurements can only be performed after the flow has relaxed from its initial perturbed state. In experiments, the trip is usually a physical device at a relatively low Reynolds number, while in simulations it more often takes the form of a synthetic inflow condition at Reynolds numbers that can be manipulated more freely. In this section, we study the minimum distance required for turbulent boundary layers to fully recover from the inflows and trips typically found in the literature.
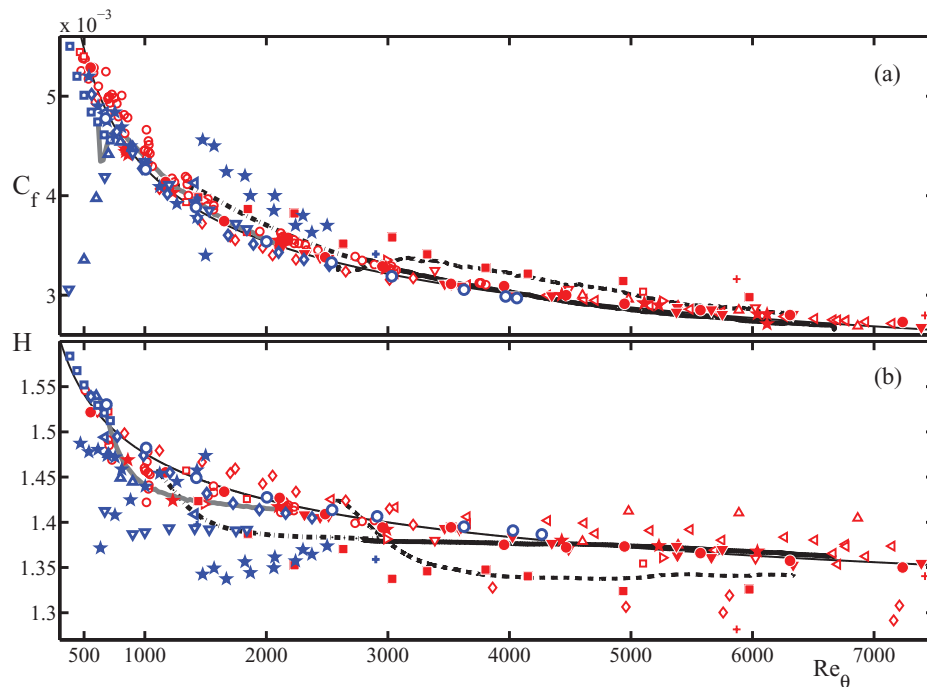
FIG. 2. (a) Friction coefficient and (b) shape factor, versus $Re_\theta$. Red symbols stand for experiments and blue for DNSs. Experiments (in red): ○,[5] ◊,[27] ◁,[28] ▷,[9] ▽,[29] △,[30] □,[31] +,[32] ★,[33] ▼,[34] ● ♦ ■.[35] DNSs (in blue): ○,[36] ◁,[37] ▽,[38] △,[39] ◊,[40] □,[41] +,[42] ★.[43] Lines are: —— (in grey) $BL_{2100}$ and $BL_{6600}$; - - - - $BL_0$; —·— $BL_{AUX}$; —— fit from Ref. 24.

Figure 2(a) displays the evolution of the friction coefficients of our boundary layers, $C_f = 2/U_\infty^{+2}$, as functions of $Re_\theta$. For comparison, it includes numerical and experimental data in the same range of $Re_\theta$, as well as the empirical correlation proposed in Ref. 24. It is seen that, after a relatively short transient in which $C_f$ increases rapidly, all the simulations tend to converge to the empirical fit. In particular, the "production" simulation $BL_{6600}$ agrees well with both numerical and experimental data, while the recoveries of the feeder simulation $BL_{AUX}$, and specially of $BL_0$, are barely complete within their computational boxes. Note that a similar initial behavior is found in many experiments in which the friction coefficient increases during transition to later decrease slowly. Although simulations and experiments are very different, that similarity can be traced to a common mechanism that is also found in simulations of decaying isotropic turbulence from random initial conditions.[44] As turbulence becomes organized from the artificial perturbations introduced either by the trip, the inflow, or the initial conditions, dissipation first grows to a maximum, that can be identified as the first moment in which the flow is truly turbulent,[5] and subsequently decreases as turbulence decays or the boundary layer thickens.

Figure 2(b) shows that the shape factor, $H = \delta^*/\theta$, is more scattered and recovers more slowly than $C_f$, both in simulations and in experiments. In our simulations, $H$ decreases at the beginning of each computational box, and recovers slowly thereafter. The auxiliary simulation $BL_{AUX}$, and especially $BL_0$, are not fully relaxed by the end of their computational boxes, but $BL_{6600}$, which benefits from the relaxation of its feeder simulation $BL_{AUX}$, is always within the experimental scatter and matches the empirical correlation in the second half of its box. In the lower-Reynolds-number case $BL_{2100}$, whose inflow is at $Re_\theta \approx 615$, the recovery is masked by the natural transition to turbulence, but it is probably also fully relaxed in the last third of the box.[15] Other experiments[5,27] and simulations show similar trends, and the figure suggests that some of the simulations available in the literature[42,43] might not be fully converged by the end of their computational boxes. The difference between the recovery rates of $C_f$, which measures a near-wall property, and $H$, which represents the whole velocity profile, suggests that the problem is the slow convergence of the larger outer scales.
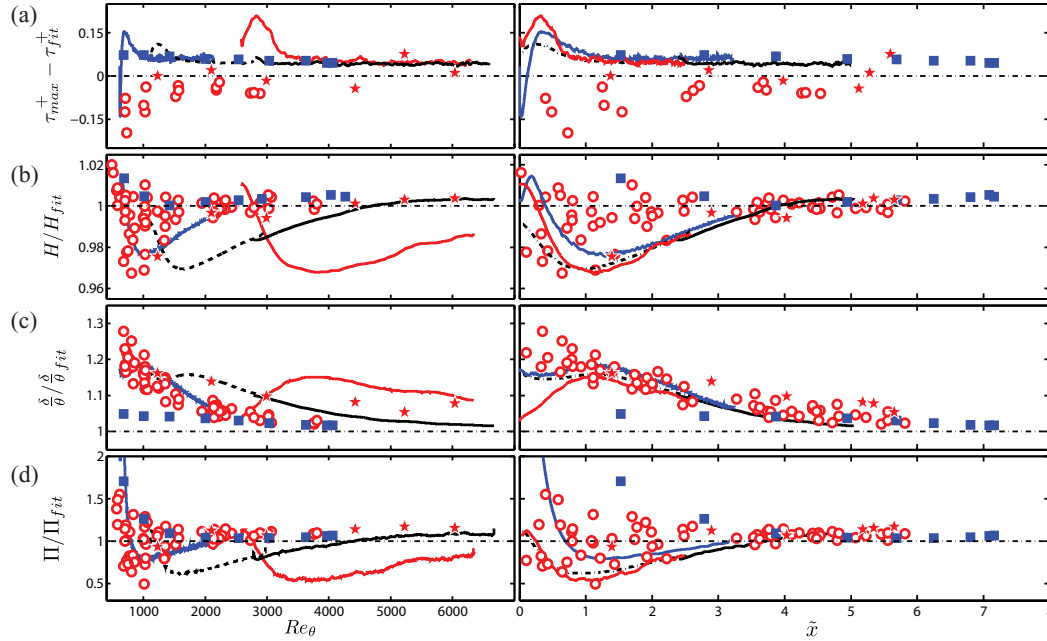
FIG. 3. Comparison of the initial evolution of (a) the maximum Reynolds stress $\tau_{max}^+$, (b) shape factor $H$, (c) $\delta/\theta$, and (d) wake intensity $\Pi$. Plotted against $Re_\theta$ on the left, and against the number of eddy turn-overs $\widetilde{x}$ on the right. Quantities are normalized with empirical fits to remove as much as possible the drift with Reynolds number. Symbols are: experiments ○ (red),[5] ★ (red),[33] and DNS ■ (blue).[36] Lines are: —— (blue) $BL_{2100}$, ---- $BL_{AUX}$, ——$BL_{6600}$, —— (red) $BL_0$, and —·— empirical fits.

It was argued in Ref. 7 that the proper length scale to characterize the recovery is the turnover length, $L_{to} = U_\infty^+ \delta$, which measures how far eddies are advected during a large-scale turnover time $\delta/u_\tau$. An effective dimensionless "turnover distance" can thus be defined as $\widetilde{x} = \int^x [\,dx/(\delta U_\infty^+)]$, integrated from the numerical inflow or from some other location characterizing the transition to turbulence. It is more common in experiments to base the relaxation criterion on the boundary layer thickness,[45] such as in $\widetilde{x}_\delta = \int^x [\,dx/\delta]$. The two criteria differ by a factor $O(U_\infty^+)$, which changes by less than 20% over the range of Reynolds number in Figure 2, so that $\widetilde{x}_\delta/\widetilde{x} \approx 21$–25 at low Reynolds numbers, but $\widetilde{x}$ has a clearer physical interpretation. Note that the boundary layer thickness increases by a factor of about 4 over the recovery distances discussed below, $\widetilde{x} \approx 4$–5, so that the thickness used for normalization becomes important. For example, if the relaxation distance is expressed in terms of the inflow boundary layer thickness, instead of the running average used above, the recovery criterion becomes $x/\delta_{in} \approx (50$–$60)\,\widetilde{x}$.

Whether the scatter with respect to the empirical correlations in Figure 2 is an effect of the low Reynolds numbers or of an incomplete recovery is tested in Figure 3, which shows the evolution of several variables in terms of $Re_\theta$ and of $\widetilde{x}$. It includes the simulations in Table I and other experimental[5,33] and numerical[36] boundary layers for which the relevant data are available. The maximum Reynolds stress, $\tau_{max}^+ = -\langle uv \rangle_{max}^+$, displayed in Figure 3(a), is a near-wall quantity attained at $y_{max}^+ = O(\delta^{+1/2})$,[46] and is therefore presumably related to the relatively small scales near the wall, but the other three variables, $H$, $\delta/\theta$, and the wake intensity $\Pi$, are outer-layer properties linked to larger scales.

The wake strength is estimated from the usual profile representation,[47]

$$U^+ = B + \frac{1}{\kappa}\ln(y^+) + \frac{\Pi}{\kappa}W(y/\delta), \qquad (1)$$

applied at $y = \delta$, where the wake function is defined as $W(1) = 2$, and the Kármán and intercept constants are taken respectively as $\kappa = 0.41$ and $B = 5$.
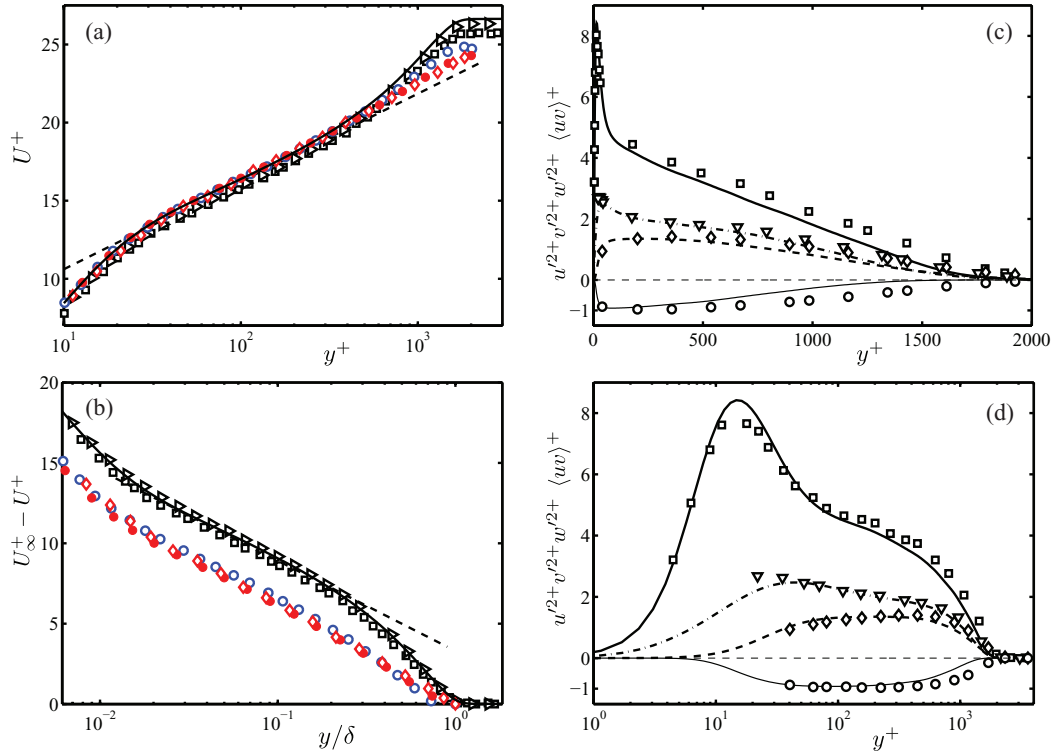
FIG. 4. Mean streamwise velocity profiles in inner (a) and outer velocity-defect forms (b). Symbols are: ● (red) CH2000; ◊[16] (red) experimental channel at $\delta^+ \approx 2000$; ◯[57] (blue) experimental pipe at $\delta^+ \approx 2000$; experimental boundary layer □[33] at $Re_\theta = 5230$ and ▷[28] at $Re_\theta = 5156$; —— $BL_{6600}$ at $Re_\theta = 5160$; - - - - $5 + \log(y^+)/0.41$ (a); - - - - $3.3 - \log(y/\delta)/0.41$ (b). (c) and (d) Profiles of Reynolds stresses at $Re_\theta = 5230$. $BL_{6600}$: —— $u'^{2\,+}$, - - - - $v'^{2\,+}$, — · — $w'^{2\,+}$, —— $\langle uv \rangle^+$. Symbols are an experiment from Ref. 33 at the same Reynolds number.

All the quantities have been normalized by empirical fits that approximate their evolution with $Re_\theta$, but which should be seen as aids intended to amplify the differences among cases rather than as theoretical models. The fits used for $H$ and $\delta/\theta$ are those in Ref. 24, and that for $\Pi$ is from Ref. 48. The model for the maximum Reynolds stress in Figure 3(a) is obtained by assuming that the total stress, $\partial U^+/\partial y^+ + \tau^+$, is equal to $1 - y/\delta$, and that the maximum of $\tau$ is within the logarithmic mean velocity profile. The first assumption is only strictly true in pipes and channels, although it is also a reasonable approximation in boundary layers (see Ref. 15 and Figure 4(c) above), while the second is questionable at low Reynolds numbers and should only be considered as a modeling artifice. The result is

$$\tau_{fit}^+ \approx 1 - 2(\kappa\delta^+)^{-1/2}, \quad \text{at} \quad y_{max}^+ \approx (\delta^+/\kappa)^{1/2}. \tag{2}$$

To unify the definition of the turnover distance, we have used the initial maximum of the friction coefficient as the origin for the integral defining $\widetilde{x}$. In the experiments for which that point is reported,[5] and in simulations forced at low Reynolds numbers to mimic a physical trip,[6,36] the maximum friction coefficient is typically attained at $Re_\theta = 400$–$600$. In experiments in which that point is not reported,[33] we have approximated it by $Re_\theta = 500$. In our simulations with synthetic inflows, the maximum of $C_f$ is available and depends on the inflow Reynolds number.

It is clear from Figure 3 that $\widetilde{x}$ collapses the initial recovery much better than $Re_\theta$, especially for the fairly wide range of inflow Reynolds numbers of the simulations. Experiments are more scattered than simulations, but all the results tend to collapse to a common behavior at roughly the same $\widetilde{x}$.

Reference 7 found that the relaxation of most flow scales requires at least $\widetilde{x} = 1$, in agreement with the results for the maximum Reynolds stress in Figure 3(a), but the other three variables in

Figures 3(b)–3(d) reveal that larger scales relax more slowly. The shape factors $H$ and $\delta/\theta$ do not converge in our DNSs until $\widetilde{x} \approx 3$–4 ($\widetilde{x}_\delta \approx 90$, or $x/\delta_{inlet} \approx 200$), and $\Pi$, which depends on the profile far from the wall and may therefore be expected to represent even larger scales than the shape factors, only recovers after $\widetilde{x} \approx 4$–5 ($\widetilde{x}_\delta \approx 120$, or $x/\delta_{inlet} \approx 250$).

Similar trends apply to experiments once the different trips have been taken into account by using the $C_f$ peak as reference. For example, Ref. 5 tested several tripping devices inducing transition around $Re_\theta \approx 500$, and concluded that their effects persist to $Re_\theta \approx 1500$, roughly $\widetilde{x} \approx 3.5$. The numerical simulations in Refs. 6 and 36, which are tripped at $Re_\theta = 180$ and peak at $Re_\theta \approx 420$, recover at $Re_\theta \approx 1000$ ($\widetilde{x} \approx 4$), and a recent re-analysis of those data and of new simulations tripped at $Re_\theta = 300$ concludes that some differences persist up to $Re_\theta \approx 2000$ ($\widetilde{x} \approx 5$).[6]

Those relaxation lengths are similar to those of $BL_{\text{AUX}} + BL_{6600}$, even if the inflow of that simulation is at a higher Reynolds number than the trips of the experiments, so that it only reaches its $C_f$ peak at $Re_\theta \approx 1100$ and $\widetilde{x} = 4$ at $Re_\theta \approx 4800$. Its agreement with the lower-Reynolds-number cases reinforces the use of the turnover distance, $\widetilde{x}$, as a recovery criterion.

Unfortunately for the cost of simulations, $L_{to}/\delta$ increases with $Re_\theta$, and simulations become increasingly expensive. For example, the computational box of the high-Reynolds number case $BL_0$ has roughly the same $L_x/\theta$ as the lower-Reynolds-number case $BL_{2100}$, but its $\widetilde{x}$ is 20% shorter. Correspondingly, as shown in Figure 2, it does not reach equilibrium within its box.

## IV. ONE-POINT STATISTICS

We next examine the one-point statistics of our boundary layers, and compare them to channels and pipes at similar Reynolds numbers. In particular, we will use numerical channels from our group at $\delta^+ = 181$ (CH180), $\delta^+ = 550$ (CH550),[12] $\delta^+ = 934$ (CH950),[49] $\delta^+ = 2003$ (CH2000),[2] and $\delta^+ = 4200$ (CH4000)[50] to remove some of the ambiguities of previous studies at lower Reynolds numbers.[14,15] For completeness, we will also use data from recent pipe simulations at moderate Reynolds numbers.[51] It should be noted that the computational box of CH4000, $L_x \times L_z = 2\pi\delta \times \pi\delta$, is smaller than those of the other four channels and, although large enough to contain the full spectra of the wall-normal and spanwise velocities,[52] it is marginal for those of the streamwise fluctuations. That could suggest some depletion of the fluctuations of the streamwise velocity, but it has been noted before that the longest scales are not really missing, but aliased into infinitely long structures,[49] with negligible effects on the one-point statistics for boxes of this size.[52] For example, Ref. 53 used a similar computational box for a channel at $\delta^+ = 590$ whose fluctuations are known to agree well with larger boxes, and the same is true for test simulations in our group at $\delta^+ = 2000$.[54]

The mean streamwise velocity in both, inner and outer velocity-defect forms,[55,56] is presented in Figures 4(a) and 4(b) for $BL_{6600}$ at $Re_\theta = 5160$, along with experimental boundary layers at $Re_\theta \approx 4980$–5230 ($\delta^+ \approx 1565$–1625), and numerical[2] and experimental[16] channels and pipes[57] at $\delta^+ \approx 2000$. The agreement among the boundary layers is satisfactory, and the weaker wake of the internal flows is evident. The wake intensity of the boundary layers, $\Pi \approx 0.57$, is already close to the classical asymptotic value $\Pi = 0.55$.[47,58] Since it was shown in Ref. 15 that the wake is a reflection of the entrainment of irrotational fluid at the edge of the boundary layer, this suggests that the entrainment has reached equilibrium at these Reynolds numbers.[58] The profile has about a decade of visually logarithmic behavior (inferred from the simultaneous overlap of the inner and outer form of the profile), although it is known that the parameters of the logarithm only reach their asymptotic values at Reynolds numbers at least an order of magnitude higher than those considered here.[59]

The mean-squared fluctuations of $BL_{6600}$ are presented in Figures 4(c) and 4(d) compared with experimental results at the same Reynolds number.[33] The abscissae of Figure 4(c) is linear, highlighting the outer region, whereas the abscissae of Figure 4(d) is logarithmic, emphasizing the near-wall and logarithmic regions. The agreement of the data is satisfactory, even if the experimental layer appears to be slightly thicker than the simulation, or if the maximum intensity of the streamwise fluctuations slightly lower.

Figures 5(a)–5(d) show semilogarithmic plots of the intensities, emphasizing both the region near the wall, and the logarithmic behavior of some of the fluctuation profiles farther away. That
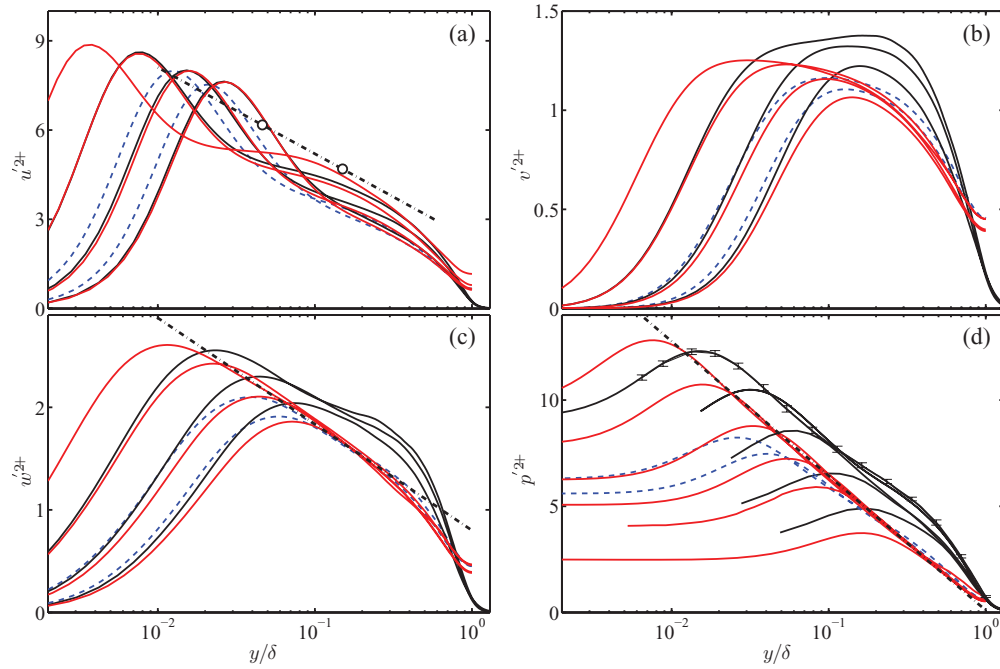
FIG. 5. Mean-squared profiles of: (a)–(c) the velocity, and (d) pressure fluctuation intensities for wall-bounded flows in the range $\delta^+ = 180$–4000. Boundary layers are in black, channels in red, and pipes in dashed blue. (a)–(c) —— Boundary layers at $\delta^+ = 550$ from $BL_{2100}$, $\delta^+ = 950$,[36] and $\delta^+ = 2000$ from $BL_{6600}$; ---- (dashed blue) pipe simulation[51] at $\delta^+ \approx 685, 1140$; —— (red) channels CH550-CH4000; —·— fits for the logarithmic region of $u'^2{}^+$ and $w'^2{}^+$. (a) Fit for $u'^2{}^+$ as in Ref. 67: $u'^2{}^+ = 2.3 - 1.26\log(y/\delta)$. The open circles mark the region $3\delta^{+1/2} < y^+ < 0.15\delta^+$ of CH4000. (c) Fit $w'^2{}^+ = 0.8 - 0.45\log(y/\delta)$. (d) Profiles of the pressure fluctuations intensities $p'^2{}^+$. Data as in (a)–(c), plus boundary layers[68] at $\delta^+ = 173$ and $\delta^+ = 280$. Channels are CH180–CH4000. Error bars are included for $BL_{6600}$. —·— fit for $p'^2{}^+ = 0.1 - 2.75\log(y/\delta)$.

behavior was predicted by Tonwsend[11,60] and, although it has been mostly analyzed in the context of a particular eddy model,[61–63] it is a general property of any self-similar hierarchy of attached eddies. In essence, "active" eddies of size $O(y)$ are assumed to be responsible for the tangential Reynolds stress in a logarithmic band of wall distances around $y$. Since the stress is $O(u_\tau^2)$ from momentum-conservation arguments, this implies that the velocity fluctuations are $O(u_\tau)$. Their contribution to the tangential stress is damped closer to the wall, but their wall-parallel velocities are not. Approaching the wall therefore results in the accumulation of energy originating from a progressively wider range of wall distances, which also corresponds to a wider range of wall-parallel sizes.[60,64,65] The scales corresponding to structures whose active cores are above the observation point are "inactive" in the sense of not carrying Reynolds stresses,[2,66] and the ratio between the energy and the stresses, which is the intensity expressed in wall units, grows as the wall is approached (see Figure 5). It follows from the self-similar structure in $y$ that the accumulated intensity is logarithmic in $y$.[11]

The first clear evidence for logarithmic intensity profiles probably came from $w'^2$ and $p'^2$ in simulations of channels[3] and boundary layers,[15] and it is evident for those two variables in Figures 5(c) and 5(d). The parameters of the logarithmic fits for the channel simulations are included in the figures, as indicated in the corresponding captions.

The logarithmic behavior of the streamwise velocity fluctuations, although easier in principle to measure, is contaminated by strong viscous effects near the wall and has taken longer to demonstrate experimentally,[18,67] although earlier indications were available from atmospheric flows.[63] Figure 5(a) presents all the available simulations, and includes the logarithmic fit proposed in Ref. 67, which, for the highest-Reynolds-number case CH4000, should apply between the two open circles added to the dashed line. Although that fit is quite convincing over the much wider range of Reynolds numbers in the experimental publication ($\delta^+ \approx 2\times10^3 - 6\times10^5$),[18,67] it is harder

to discern in the present simulations ($\delta^+ \approx 4 \times 10^3$), or in previous experiments, highlighting the difficulties involved in studying a property applying only to a range of very-high Reynolds numbers that is hard to measure experimentally, and which is out of the reach of the current generation of numerical simulations.

Figure 5(b) presents the fluctuations of the wall-normal velocity, which are not expected to have a logarithmic range because they are blocked by the wall.[11] They do not behave logarithmically in the figure, and their slight growing trend towards the wall can be absorbed by normalizing them with the local mean tangential total stress, instead of with a global friction velocity.[69] Since the total tangential stress decreases linearly in channels with the distance to the wall, but not in boundary layers, at least near the wall, $v'^2$ is correspondingly much closer to being constant in the latter than in the former.

The most interesting aspect of Figure 5 is the comparison between boundary layers, channels, and pipes. It has been known for some time that the transverse velocity components and the pressure are more intense in boundary layers that in channels when scaled with the friction velocity,[15] and Figure 5 confirms that the difference is between internal and external flows,[14] since pipes follow the same trends as channels. The figure also shows that the differences between the two kinds of flows concentrate in a "hump" around $y/\delta = 0.3$–0.8, which appears to saturate for the highest Reynolds numbers. Even the pressure fluctuations seem to be developing such a hump in the outer layer, which was not present at the Reynolds numbers in Ref. 15, and which is neither found in the internal flows. That hump is subtle, but it is probably real, because it is present at the two higher Reynolds numbers, which originate from different groups and different simulation codes, and is much stronger than the uncertainties of the data. The error bars added to $BL_{6600}$, defined as in Ref. 70, are comparable to the thickness of the line.

The difference between internal and external flows is less obvious for the streamwise velocity fluctuations,[14,15] and it was unclear in previous studies whether there was any difference at all. It turns out that the problem is a representation artifact due to the different magnitudes of the three velocity components, which hide increments in Figure 5(a) that are of the same order as those in the other figures.[71]

This is shown in Figure 6, which documents that the differences between boundary layers and channels are very similar for $u'^2$ and $v'^2$, while only those of $w'^2$ are slightly larger. The maximum differences occur at $y/\delta \approx 0.35$ for the transverse velocities and at $y/\delta \approx 0.5$ for $u'^2$, which is in the same general range as the hump in $p'^2$. The two effects are presumably related, and the fact that the velocity differences are roughly isotropic, rather than having the same fractional increments, is consistent with the idea that they are due to the rotational-irrotational intermittency at the edge of
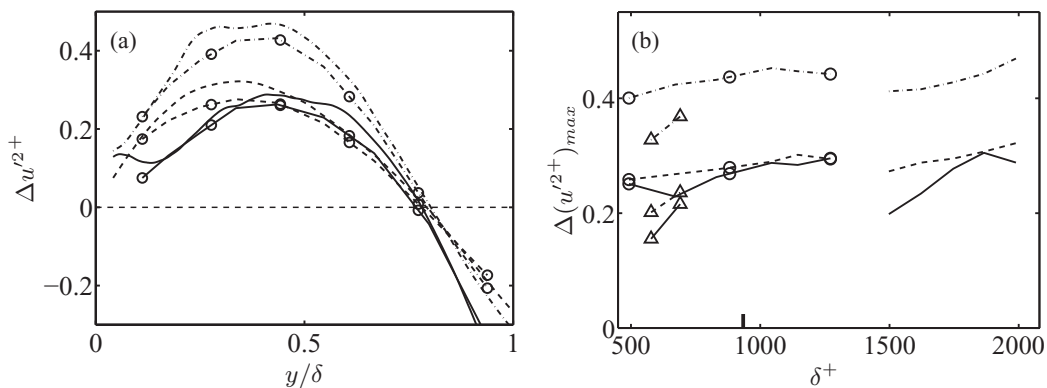


FIG. 6. (a) Difference of the squared intensities between boundary layers and channels, $\Delta u'^{2+} = u'^{2+}_{BL} - u'^{2+}_{CH}$, for the three velocity components. Lines without symbols are $BL_{6600}$ ($\delta^+ = 1900$) compared with CH2000 ($\delta^+ = 2000$); and those with circles are Ref. 36 ($\delta^+ = 1000$) compared with C950 ($\delta^+ = 935$). (b) Maximum difference of the squared intensities between boundary layers and channels. $\triangle$ $BL_{2100}$; $\bigcirc$ Ref. 36; lines without symbols $BL_{6600}$. The tick mark at the horizontal axis near $\delta^+ = 950$ is the order of magnitude of the error made in interpolating CH950 from CH550 and CH2000. In both panels: ——$u$, - - - - $v$, — · — $w$.
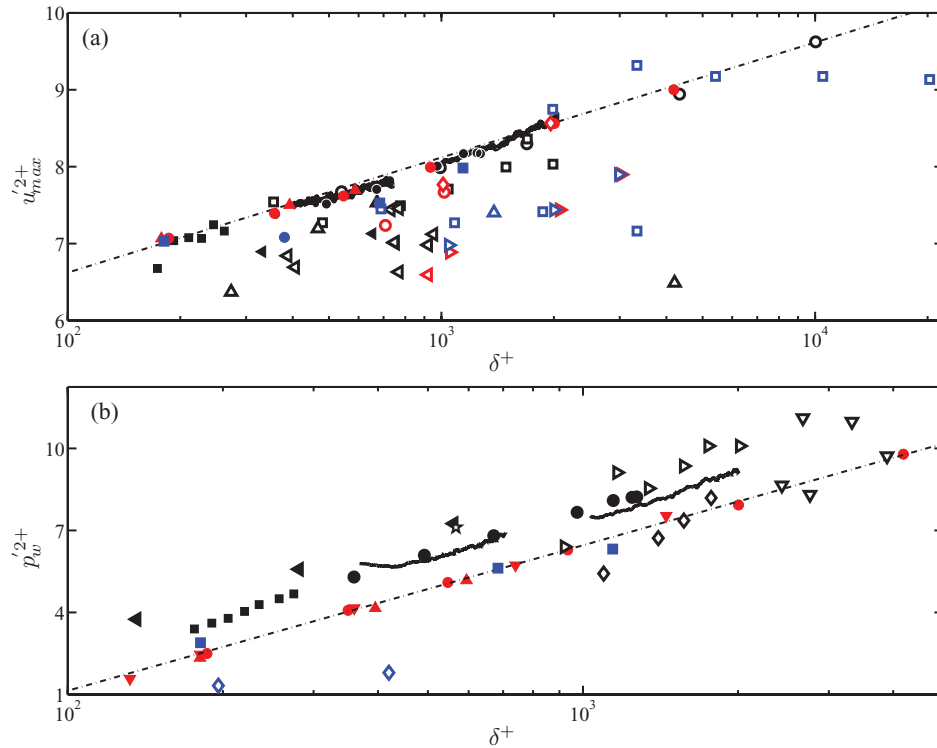
FIG. 7. Maxima of the mean-squared: (a) streamwise velocity fluctuations $u_{max}'^{2+}$, and (b) wall-pressure fluctuations $p_w'^{2+}$, as functions of $\delta^+$. Internal flows are colored in red (channels) and blue (pipes), while external flows (boundary layers) are colored in black. Filled symbols stand for numerical simulations and empty ones for experiments. Channels (in red): ●,[2, 12, 49] ▲,[53] ▼,[74] ◁,[75] ◯,[76] ◇,[16] ▷.[4] Boundary layers: ■,[68] ●,[36] ◀,[37] □,[33] ◯,[9] ◁,[5] △,[30] ▷,[77] ▽,[78] ★,[79] ◇.[32] Pipes (in blue): ■,[51] ●,[80] □,[17,18] ▷,[4] △,[81] ◇.[82] Solid lines are the numerical boundary layers $BL_{2100}$ and $BL_{6600}$. —·— fits for numerical channels CH180–CH4000: $u_{max}'^{2+} = 3.63 + 0.65\log(\delta^+)$ and $p_w'^{2+} = -9.5 + 2.31\log(\delta^+)$.

the boundary layer. An isotropic acceleration suggests the effect of pressure, which is the only force able to act on the irrotational flow being engulfed from the free stream into the turbulent layer.[15] Figure 6(a) contains two Reynolds numbers that agree well, and Figure 6(b) shows that the maximum differences for the three velocity components are essentially independent of the Reynolds number. If we admit that the wake component of the mean velocity, the pressure hump, and the fluctuation excesses are all consequences of the entrainment of irrotational fluid, Figure 6(b) is consistent with the observation that the wake component has reached its asymptotic value at the Reynolds number of $BL_{6600}$, and suggests that the same should be true for the magnitude of the pressure hump.

A consequence of the logarithmic behavior of the attached flow variables is that they reach their maximum values near the wall, and that those maxima increase with $\delta^+$.

The logarithmic increase of the maximum streamwise velocity $u_{max}'^{2+}$, which is attained at $y^+ \approx 15$, was first documented experimentally in Ref. 9, and has been confirmed since then as the Reynolds numbers of experiments and simulations have steadily increased.[2, 4, 10, 72, 73] Figure 7(a) is a compilation of the latest available data for the three canonical flows. A similar compilation for the pressure at the wall is given in Figure 7(b), which shows both the logarithmic trend with $\delta^+$ and the different additive constants for internal and external flows.

Unfortunately, the experimental confirmation of the logarithmic trend of $u'^{2+}_{max}$ has not been free from controversy, most likely because of the difficulty of measuring so close to the wall. The simulation data represented by heavy lines or by solid symbols in Figure 7(a) follow the logarithmic trend very well, while the open symbols of the experiments are very scattered, falling mostly below the simulations. This suggests that the problem is likely due to instrumental limitations brought about by sensors that filter part of the energy. The problem has long been recognized by experimentalists[83]

and it is common to apply corrections to try to compensate for it, some of which may introduce new errors. This, for example, may be the case for the highest-Reynolds-number cases included in Figure 7(a), which are the pipe-flow measurements[18] represented by the open blue squares around $\delta^+ = 10^4$. They initially exceed the DNS trend line, and later fall below it as they remain independent of the Reynolds number, but they have been corrected to compensate for sensor size.[84] In fact, a previous experiment by the same group, using the same facility at somewhat lower Reynolds numbers, had found uncorrected intensities that were also independent of $\delta^+$, but that were lower than their higher-Reynolds-number ones.[17] Those data are included in Figure 7(a), in the range $\delta^+ = 700$–3000, using the same symbols as for the high-Reynolds number case. The two sets differ by about 20% when they overlap around $\delta^+ \approx 3000$ and, although some reconciliation can be achieved by either correcting the low-Reynolds-number cases or uncorrecting the high-Reynolds-number ones, substantial differences remain. It is also interesting to note that, when the low-Reynolds number pipe cases were repeated by a different group in a different facility,[4] they were found to increase logarithmically with the Reynolds number, although at a slightly lower level than the simulations ($\triangleright$ (blue) in Figure 7(a)), and that the open circle at $\delta^+ \approx 10^4$ in Figure 7(a) is an experimental boundary layer that follows well the logarithmic trend. Although it is possible that different flows have different near-wall behaviors, and that pipes are different from other flows, the logarithmic profile mentioned above for $u'^2$ was identified in pipes,[18] and it would have to fail near the wall for the maximum fluctuations to be independent of the Reynolds number. It is precisely near the wall where the flow dynamics are expected to be less dependent of the type of flow. In summary, given the evidence collected in Figure 7(a) from the present and previous simulations and experiments, it is probably safe to conclude that the inner streamwise-velocity peak increases logarithmically with the Reynolds number, as predicted by the theory,[60] and that the experimental scatter is due to measurement limitations. That is particularly true below $\delta^+ \approx 5000$, where more than one data set is available.

In fact, if the location of the maximum fluctuations is known, the logarithmic profiles as a function of $y$ can be directly related to the evolution of the maximum intensity as a function of $\delta^+$. Thus, the pressure profile for channels in Figure 5(d), $p'^{2+} = 0.1 + 2.75\log(\delta/y)$, is approximately consistent with the behavior of the pressure at the wall in Figure 7(b), $p_w'^{2+} = -9.5 + 2.31\log(\delta^+)$, if we assume that the wall pressure is reached at a constant $y^+ \approx 50$, which has been independently confirmed. A similar identification can be made for the spanwise velocity component, because in both cases the coefficient of the logarithm in the formula for the profile as a function of $y$ and in the one for the peak intensity as a function of $\delta^+$ are roughly equal.

The case of $u'^{2+}$ is more interesting because the coefficients on the logarithmic terms in fits for $u'^{2+}_{max} \sim 0.65\log(\delta^+)$ (see Fig. 7) and $u'^{2+} \sim 1.26\log(\delta/y)$[67] differ roughly by a factor of two. Applying the argument above would in this case suggest that in the limit of high $\delta^+$, the maximum intensity is reached at $y^+ \sim \delta^{+1/2}$. This is obviously not true, since experiments and simulations show that the maximum is reached near $y^+ = 15$, independent of $\delta^+$. But it is consistent with the tentative conclusion in Ref. 67 that the logarithmic fluctuation profile is only found above a "mesolayer" extending from the edge of the viscous region to $y^+ \approx 3\,\delta^{+1/2}$.

The value of $u'^{2+}$ at the outer edge of this mesolayer must thus scale like $0.63\log(\delta^+)$ for large $\delta^+$. This accounts for the variation of $u'^{2+}_{max}$ with $\delta^+$ if we assume there is a roughly Reynolds number independent additive contribution to the $u'^{2+}$ profile below the mesolayer outer edge. To test this hypothesis, $u'^{2+} - u^{2+}_{max}$ is plotted in Fig. 8, where the outer edge of the mesolayer is indicated with a circle for each curve. The profiles for all cases collapse reasonably well, except for near the outer edge of the mesolayer, where the increase with $\delta^+$ of the width of the mesolayer, in wall units, must be accommodated. Note in particular that the value of $u'^{2+} - u^{2+}_{max}$ at the outer edge of the mesolayer (circles in Fig. 8) varies much less with Reynolds number than $u^{2+}_{max}$. The three kinds of flows collapse extremely well in this very-near-wall region. Reference 67 suggests that, at extremely high Reynolds numbers, the upper end of the mesolayer develops an outer peak of $u'^2$, which is absent in Figure 8. But, the Reynolds number of the simulations are too low to say anything about that possibility, and the resolution limits discussed above for those experiments recommend caution.

The reason for the behavior of $u'^{2+}$ in the mesolayer is not clear. It was originally proposed to extend below the location of the maximum Reynolds stress,[46,85] because the viscous stress has to
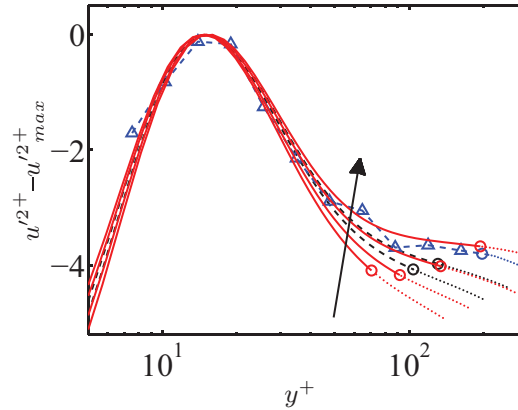
FIG. 8. Inner peak of the streamwise velocity fluctuations, in wall scaling and subtracting the maximum for each case. Each line is restricted to $y^+ \leq 3\delta^{+1/2}$, marked by a circle. The Reynolds number increases in the direction of the arrow. ——— (red) numerical channels CH550–CH4000; - - - - $BL_{6600}$ at $\delta^+ = 1200$ and 1900; $\triangle$ (blue) experimental boundary layer at $\delta^+ = 4338$.[9]

be taken into account in that region. While that is clearly true for the mean profile, it is harder to understand how fluctuations can be directly influenced by viscous accelerations. Consider an eddy of size $O(y)$ and intensity $O(u_\tau)$, which undergoes accelerations of order $u\nabla u = O(u_\tau^2/y)$ due to forces per unit mass of the same order. The ratio of those forces to the mean viscous force, $\nu\partial_{yy}U \approx \nu u_\tau/\kappa y^2$, is $O(y^+)$, implying that the mean viscous force, even if important for the mean profile, is probably always negligible for the fluctuations above the buffer layer. Smaller eddies suffer even higher accelerations.

An explanation could be that the mesolayer effect on the fluctuations is simply the reflection of a different scaling velocity, once the average tangential Reynolds stress decreases below $u_\tau^2$. The structure of the flow could still be the same, but the logarithmic argument ceases to hold once the requirement that $-\langle uv \rangle$ should be proportional to $u_\tau^2$ is removed. For example, it can be shown that the stress-structure coefficient, $c_{uv} = -\langle uv \rangle/u'v'$, which can be taken as an indication of the momentum-transferring mechanism of the active eddies, does not change appreciably over the mesolayer, and neither does $w'^{2+}$, suggesting that the structure of the eddies does not change. It is also suggestive that the edge of the mesolayer is always close to the maximum of $v'^2$, but attempting to scale $v'^2$ with $\langle uv \rangle$ works poorly.

Any further understanding of this region will have to wait until either detailed experimental measurements or simulations become available at Reynolds numbers high enough for the mesolayer, if it indeed exists, to become longer and more noticeable than at present.

## V. CONCLUSIONS

A new direct numerical simulation of a zero-pressure-gradient boundary layer in the range $Re_\theta = 2780–6680$ has been presented and compared with corresponding channel and pipe flows in the comparable Reynolds-number range $\delta^+ \approx 1000–2000$.

We have shown that the eddy turn-over length[7] $\tilde{x}$ is the appropriate scale to characterize the recovery of the different flow-scales after the initial trips and inflow conditions typically found in the literature, rather than $Re_\theta$. Parameters linked to the large-scales, such as the shape factor or the wake parameter of the mean velocity profile, only recover after $\tilde{x} \approx 4–5$, which is equivalent to 100–120 mean boundary-layer thickness, or to 250 boundary-layer thicknesses measured at the inflow. Shorter distances $\tilde{x} \approx 1$ are needed for the parameters related to small-scales, such as the maximum Reynolds stresses. Since the eddy turn-over length increases with the Reynolds number, simulations initiated at higher Reynolds numbers become increasingly expensive. To avoid this penalty, we use a double-simulation-box strategy to maximize $\tilde{x}$ within reasonable cost, concluding that all the scales in our simulation are correctly represented for $Re_\theta > 4800$.

One-point statistics, represented by the mean velocity profile and velocity fluctuations, agree well with the boundary layers surveyed in this paper. For Reynolds numbers $\delta^+ \approx 2000$, clear evidence of the existence of logarithmic fluctuation profiles are found for $w'^{2+}$ and $p'^{2+}$, both in boundary layers and in channels. An attempt was made to confirm the logarithmic profile proposed by Marusic et al.[67] for the streamwise velocity fluctuations, using channels up to $\delta^+ \approx 4000$, but even that Reynolds number seems too low to corroborate or reject its existence. One of the consequences of the logarithmic profiles of these attached variables is that the maximum value of their fluctuation intensities depends on the Reynolds number and is reached near the wall. We have confirmed that the maximum of $u'^{2+}$ and the value of $p'^{2+}$ at the wall are proportional to $\log(\delta^+)$. The same is true for $w'^{2+}_{max}$. In some of those cases, such as in the logarithmic growth of $p'^{2+}_w$ and $w'^{2+}_{max}$ with $\delta^+$, the behavior is consistent with a fixed location for the maximum at some fixed value of $y^+$. On the other hand, the maximum of the streamwise velocity fluctuations can probably only be understood by accepting the conclusion in Ref. 67 that the logarithmic fluctuation profile only exists above a mesolayer[46] extending up to $y^+ = 3\,\delta^{+1/2}$. In agreement with previous observations,[3] no evidence of a logarithmic profile is observed for the wall-normal velocity.

Comparison of external and internal flows confirms that, when scaled with the friction velocity, the transverse velocities and pressure fluctuations are more intense in boundary layers, as originally found by Jiménez and Hoyas,[3] and we have shown that the same is true for the streamwise velocity fluctuations. The excesses of the three velocity components with respect to channels are of the same order, and reach a maximum around $y/\delta = 0.35$–0.5, essentially independently of the Reynolds number. This has been argued to be consistent with the notion that those differences originate as a consequence of the entrainment of irrotational fluid in boundary layers,[15] which is absent from internal flows.

## ACKNOWLEDGMENTS

[1] J. Kim, P. Moin, and R. Moser, "Turbulence statistics in fully developed channel flow at low Reynolds number," J. Fluid Mech. **177**, 133–166 (1987).

[2] S. Hoyas and J. Jiménez, "Scaling of the velocity fluctuations in turbulent channels up to $Re_\tau = 2003$," Phys. Fluids **18**, 011702 (2006).

[3] J. Jiménez and S. Hoyas, "Turbulent fluctuations above the buffer layer of wall-bounded flows," J. Fluid Mech. **611**, 215–236 (2008).

[4] H. Ng, J. Monty, N. Hutchins, M. Chong, and I. Marusic, "Comparison of turbulent channel and pipe flows with varying Reynolds number," Exp. Fluids **51**, 1261–1281 (2011).

[5] L. Erm and P. Joubert, "Low-Reynolds-number turbulent boundary layers," J. Fluid Mech. **230**, 1–44 (1991).

[6] P. Schlatter and R. Örlü, "Turbulent boundary layers at moderate Reynolds numbers: Inflow length and tripping effects," J. Fluid Mech. **710**, 5–34 (2012).

[7] M. Simens, J. Jiménez, S. Hoyas, and Y. Mizuno, "A high-resolution code for turbulent boundary layers," J. Comput. Phys. **228**, 4218–4231 (2009).

[8] J. Hinze, *Turbulence*, 2nd ed. (McGraw-Hill, 1975).

[9] D. De Graaf and J. Eaton, "Reynolds number scaling of the flat-plate turbulent boundary layer," J. Fluid Mech. **422**, 319–346 (2000).

[10] M. Metzger and J. Klewicki, "A comparative study of near-wall turbulence in high and low Reynolds number boundary layers," Phys. Fluids **13**, 692–701 (2001).

[11] A. Townsend, *The Structure of Turbulent Shear Flows*, 2nd ed. (Cambridge University Press, 1976).

[12] J. del Alamo and J. Jiménez, "Spectra of the very large anisotropic scales in turbulent channels," Phys. Fluids **15**, L41–L44 (2003).

[13] J. Morrison, B. McKeon, W. Jiang, and A. Smits, "Scaling of the streamwise velocity component in turbulent pipe flow," J. Fluid Mech. **508**, 99–131 (2004).

[14] M. Buschmann and M. Gad-el-Hak, "Normal and cross-flow Reynolds stresses: Differences between confined and semi-confined flows," Exp. Fluids **49**, 213–223 (2010).

[15] J. Jiménez, S. Hoyas, M. Simens, and Y. Mizuno, "Turbulent boundary layers and channels at moderate Reynolds numbers," J. Fluid Mech. **657**, 335–360 (2010).

[16] M. Schultz and K. Flack, "Reynolds-number scaling of turbulent channel flow," Phys. Fluids **25**, 025104 (2013).

[17] M. Hultmark, S. Bailey, and A. Smits, "Scaling of near-wall turbulence in pipe flow," J. Fluid Mech. **649**, 103–113 (2010).

[18] M. Hultmark, M. Vallikivi, S. Bailey, and A. Smits, "Turbulent pipe flow at extreme Reynolds numbers," Phys. Rev. Lett. **108**, 094501 (2012).

[19] J. Lee and H. Sung, "Comparison of very-large-scale motions of turbulent pipe and boundary layer simulations," Phys. Fluids **25**, 045103 (2013).

[20] J. Kim and P. Moin, "Application of a fractional-step method to incompressible Navier-Stokes equations," J. Comput. Phys. **59**, 308–323 (1985).

[21] S. Nagarajan, S. Lele, and J. Ferziger, "A robust high-order compact method for large eddy simulation," J. Comput. Phys. **191**, 329–419 (2003).

[22] P. Spalart, R. Moser, and M. Rogers, "Spectral methods for the Navier-Stokes equations with one infinite and two periodic directions," J. Comput. Phys. **96**, 297–324 (1991).

[23] T. Lund, X. Wu, and K. Squires, "Generation of turbulent inflow data for spatially-developing boundary layer simulations," J. Comput. Phys. **140**, 233–258 (1998).

[24] P. Monkewitz, K. Chauhan, and H. Nagib, "Self-consistent high-Reynolds-number asymptotics for zero-pressure-gradient turbulent boundary layers," Phys. Fluids **19**, 115101 (2007).

[25] H. Nagib, K. Chauhan, and P. Monkewitz, "Approach to an asymptotic state for zero pressure gradient turbulent boundary layers," Philos. Trans. R. Soc. London, Ser. A **365**, 755–770 (2006).

[26] G. Borrell, J. Sillero, and J. Jiménez, "A code for direct numerical simulation of turbulent boundary layers at high Reynolds numbers in BG/P supercomputers," Comput. Fluids **80**, 37–43 (2013).

[27] M. Hites, "Scaling of high-Reynolds number turbulent boundary layers in the National Diagnostic Facility," Ph.D. thesis (Illinois Inst. of Technology, 1997).

[28] J. Österlund, "Experimental studies of zero pressure-gradient turbulent boundary layer flow," Ph.D. thesis (Kungl Tekniska Högskolan, 1999).

[29] T. Farabee and M. Casarella, "Measurements of fluctuating wall pressure for separated/reattached boundary layer flows," Trans. ASME, J. Vib., Acoust., Stress, Reliab. Des. **108**, 301–307 (1986).

[30] R. Smith, "Effect of Reynolds number on the structure of turbulent boundary layers," Ph.D. thesis (Princeton University, USA, 1994).

[31] L. Purtell, P. Klebanoff, and F. Buckley, "Turbulent boundary layers at low Reynolds numbers," Phys. Fluids **24**, 802–811 (1981).

[32] Y. Tsuji, J. Fransson, P. Alfredsson, and A. Johansson, "Pressure statistics and their scaling in high-Reynolds-number turbulent boundary layers," J. Fluid Mech. **585**, 1–40 (2007).

[33] H. Osaka, T. Kameda, and S. Mochizuki, "Re-examination of the Reynolds-number-effect on the mean flow quantities in a smooth wall turbulent boundary layer," JSME Int. J., Ser. B **41**, 123–129 (1998).

[34] R. Örlü and P. Alfredsson, "On spatial resolution issues related to time-averaged quantities using hot-wire anemometry," Exp. Fluids **49**, 101–110 (2010).

[35] D. Coles, "The young people's guide to the data," in *Proceedings of the Stanford Conference on Computation of Turbulent Boundary Layers, Stanford, CA*, edited by D. E. Coles and E. A. Hirst (AFOSR-IFP, 1968), Vol. 2, pp. 1–45.

[36] P. Schlatter and R. Örlü, "Assessment of direct numerical simulation data of turbulent boundary layers," J. Fluid Mech. **659**, 116–126 (2010).

[37] P. Spalart, "Direct simulation of a turbulent boundary layer up to $Re_\theta = 1410$," J. Fluid Mech. **187**, 61–98 (1987).

[38] X. Wu and P. Moin, "Transitional and turbulent boundary layer with heat transfer," Phys. Fluids **22**, 085105 (2010).

[39] X. Wu and P. Moin, "Direct numerical simulation of turbulence in a nominally-zero-pressure-gradient flat-plate boundary layer," J. Fluid Mech. **630**, 5 (2009).

[40] S. Lee and H. Sung, "Direct numerical simulation of the turbulent boundary layer over a rod-roughened wall," J. Fluid Mech. **584**, 125 (2007).

[41] M. Skote, J. Haritonides, and D. Henningson, "Varicose instabilities in turbulent boundary layers," Phys. Fluids **14**, 2309–2323 (2002).

[42] A. Ferrante and S. Elghobashi, "Reynolds number effect on drag reduction in a microbubble-laden spatially developing turbulent boundary layer," J. Fluid Mech. **543**, 93–106 (2005).

[43] G. Khujadze and M. Oberlack, "DNS and scaling laws from new symmetry groups of ZPG turbulent boundary layer flow," Theor. Comput. Fluid Dyn. **18**, 391–411 (2004).

[44] S. Orszag and G. Patterson, "Numerical simulation of three-dimensional homogeneous isotropic turbulence," Phys. Rev. Lett. **28**, 76–79 (1972).

[45] F. Clauser, "The turbulent boundary layer," Adv. Appl. Mech. **4**, 1–51 (1956).

[46] J. Klewicki, P. Fife, T. Wei, and P. McMurtry, "A physical model of the turbulent boundary layer consonant with mean momentum balance structure," Philos. Trans. R. Soc. London, Ser. A **365**, 823–839 (2007).

[47] D. Coles, "The law of the wake in the turbulent boundary layer," J. Fluid Mech. **1**, 191–226 (1956).

[48] G. Huffman and P. Bradshaw, "A note on von Kármán's constant in low Reynolds number turbulent flows," J. Fluid Mech. **53**, 45–60 (1972).

[49] J. del Alamo, J. Jiménez, P. Zandonade, and R. Moser, "Scaling of the energy spectra of turbulent channels," J. Fluid Mech. **500**, 135–144 (2004).

[50] A. Lozano-Durán and J. Jiménez, "Time-resolved evolution of coherent structures in turbulent channels," Bull. Am. Phys. Soc. **57**(17), D20.1 (2012); this channel uses the same simulation code as CH2000.

[51] X. Wu and P. Moin, "A direct numerical simulation study on the mean velocity characteristics in turbulent pipe flow," J. Fluid Mech. **608**, 81–112 (2008).

[52] O. Flores and J. Jiménez, "Hierarchy of minimal flow units in the logarithmic layer," Phys. Fluids **22**, 071704 (2010).

[53] R. Moser, J. Kim, and N. Mansour, "Direct numerical simulation of turbulent channel flow up to $Re_\tau = 590$," Phys. Fluids **11**, 943–945 (1999).

[54] A. Lozano-Durán, private communication (2012).

[55] T. Von Kármán, *Mechanische Ähnlichkeit und Turbulenz*, Sonderdrucke aus den Nachrichten von der Gesellschaft der Wissenschaften zu Göttingen: Mathematisch-physische Klasse (Weidmannsche Buchh., 1930).

[56] H. Tennekes and J. L. Lumley, *A First Course on Turbulence* (MIT Press, 1972).

[57] B. McKeon, J. Li, W. Jiang, J. Morrison, and A. Smits, "Further observations on the mean velocity distribution in fully developed pipe flow," J. Fluid Mech. **501**, 135–147 (2004).

[58] J. Murlis, H. Tsai, and P. Bradshaw, "The structure of turbulent boundary layers at low Reynolds numbers," J. Fluid Mech. **122**, 13–56 (1982).

[59] Y. Mizuno and J. Jiménez, "Mean velocity and length-scales in the overlap region of wall-bounded turbulent flows," Phys. Fluids **23**, 085112 (2011).

[60] A. Townsend, "Equilibrium layers and wall turbulence," J. Fluid Mech. **11**, 97–120 (1961).

[61] A. Perry and M. Chong, "On the mechanism of wall turbulence," J. Fluid Mech. **119**, 173–217 (1982).

[62] A. Perry, S. Henbest, and M. Chong, "A theoretical and experimental study of wall turbulence," J. Fluid Mech. **165**, 163–199 (1986).

[63] G. Kunkel and I. Marusic, "Study of the near-wall-turbulent region of the high-Reynolds-number boundary layer using atmospheric data," J. Fluid Mech. **548**, 375–402 (2006).

[64] J. Jiménez, J. del Alamo, and O. Flores, "The large-scale dynamics of near-wall turbulence," J. Fluid Mech. **505**, 179–199 (2004).

[65] J. Jiménez, "Cascades in wall-bounded turbulence," Annu. Rev. Fluid Mech. **44**, 27–45 (2012).

[66] P. Bradshaw, "Irrotational fluctuations near a turbulent boundary layer," J. Fluid Mech. **27**, 209–230 (1967).

[67] I. Marusic, J. Monty, M. Hultmark, and A. Smits, "On the logarithmic region in wall turbulence," J. Fluid Mech. **716**, R3 (2013).

[68] M. Skote and D. Henningson, "Direct numerical simulation of a separated turbulent boundary layer," J. Fluid Mech. **471**, 107–136 (2002).

[69] F. Tuerke and J. Jiménez, "Simulations of turbulent channels with prescribed velocity profiles," J. Fluid Mech. **723**, 587–603 (2013).

[70] S. Hoyas and J. Jiménez, "Reynolds number effects on the Reynolds-stress budgets in turbulent channels," Phys. Fluids **20**, 101511 (2008).

[71] J. Jiménez and R. García-Mayoral, "Direct simulations of wall-bounded turbulence," in *Direct and Large-Eddy Simulation VIII*, edited by H. Kuerten, B. Geurts, V. Armenio, and J. Fröhlich (Springer, Netherlands, 2011), pp. 3–8.

[72] M. Metzger, J. Klewicki, K. Bradshaw, and R. Sadr, "Scaling of near-wall axial turbulent stress in the zero pressure gradient boundary layer," Phys. Fluids **13**, 1819–1821 (2001).

[73] I. Marusic and G. Kunkel, "Streamwise turbulence intensity formulation for flat-plate boundary layers," Phys. Fluids **15**, 2461–2464 (2003).

[74] Z. Hu, C. Morfey, and N. Sandham, "Wall pressure and shear stress spectra from direct simulations of channel flow," AIAA J. **44**, 1541–1549 (2006).

[75] M. Niederschulte, "Turbulent Flow Through a Rectangular Channel," Ph.D. thesis (University of Illinois, Dept. of Theor. and App. Mech., 1989).

[76] T. Wei and W. Willmarth, "Reynolds-number effects on the structure of a turbulent channel flow," J. Fluid Mech. **204**, 57–95 (1989).

[77] T. Farabee and M. Casarella, "Spectral features of wall pressure fluctuations beneath turbulent boundary layers," Phys. Fluids **3**, 2410–2419 (1991).

[78] M. Bull and A. Thomas, "High frequency wall-pressure fluctuations in turbulent boundary layers," Phys. Fluids **19**, 597–599 (1976).

[79] G. Schewe, "On the structure and resolution of wall-pressure fluctuations associated with turbulent boundary-layer flow," J. Fluid Mech. **134**, 311–328 (1983).

[80] P. Loulou, "Direct simulation of incompressible pipe flow using a B-spline spectral method," Ph.D. thesis (Department of Aeronautics and Astronautics, SUDAAR 683, Stanford University, 1996).

[81] J. den Toonder and F. Nieuwstadt, "Reynolds number effects in a turbulent pipe flow for low to moderate Re," Phys. Fluids **9**, 3398–3409 (1997).

[82] G. Lauchle and M. Daniels, "Wall-pressure fluctuations in turbulent pipe flow," Phys. Fluids **30**, 3019–3024 (1987).

[83] P. Ligrani and P. Bradshaw, "Spatial resolution and measurement of turbulence in the viscous sublayer using subminiature hot-wire probes," Exp. Fluids **5**, 407–417 (1987).

[84] A. Smits, J. Monty, M. Hultmark, S. Bailey, N. Hutchins, and I. Marusic, "Spatial resolution correction for wall-bounded turbulence measurements," J. Fluid Mech. **676**, 41–53 (2011).

[85] R. Long and T.-C. Chen, "Experimental evidence for the existence of the mesolayer in turbulent systems," J. Fluid Mech. **105**, 19–59 (1981).